Hemodynamic changes induced by stenting in elastic arteries

By F. Nicoud †

1. Motivation and objectives

Angioplasty, with or without endovascular stenting, is a promising, minimally-invasive technique that can be used as treatment of occlusive disease in medium to large arteries. It has been applied extensively in the coronary, renal, and peripheral vascular systems. The use of intravascular stents tends to lower the complication rate. Although re-stenosis rates as high as 15-30 % after six months for human coronary arteries have been observed; see e.g. Rau *et al.* (1998). One possible explanation for this observation relies on the hemodynamic modifications induced by the prosthesis. Changes in wall shear stress are believed to induce endothelial dysfunction, ultimately leading to intimal hyperplasia and re-stenosis. Davies *et al.* (2001) suggest that magnitude of the shear stress is of secondary importance to the spatial and temporal fluctuations of this quantity.

In vivo testing performed by Vernhet *et al.* (2001), Vernhet *et al.* (2000), Rolland, Charifi & Verrier (1999) show that endovascular stenting induces a large modification of the arterial compliance and thus may drastically modify the propagation of arterial waves by introducing artificial reflexions. The first objective of this study is therefore to assess the amount of pressure-wave reflexion related to the endovascular stenting of an elastic artery. For this purpose, the stented section of the vessel is modeled as an elastic duct, whose compliance is less than the non-stented artery. We intent to clarify the extent of reflexion that can be expected, depending on the characteristics of both the stent and the host vessel. Another expected effect of the compliance mismatch induced by stenting is to modify the details of the blood motion in the stented area. Specifically, the wall shear stress (averaged over the cardiac cycle) might be changed, as well as the level of its systo-diastolic variations. For high enough Reynolds numbers, one also expects recirculation zones to appear with larger residence times. The second objective of this paper is thus to clarify the changes in the blood motion that can be expected in relation to endovascular stenting. Note that this study deals with the global effect of the compliance mismatch, neglecting the details of the prosthesis structure (struts). Consistently, the prosthesis is modeled as a uniform (elastic) tube with its own compliance.

2. The pressure-wave point of view

2.1. *Basic equations*

The general one-dimensional (1D) equations describing the pulsatile blood flow (mass and momentum conservation) in compliant arteries are well known since the work of Hughes & Lubliner (1973):

$$\frac{\partial A}{\partial t} + \frac{\partial Au}{\partial x} = 0, \qquad \frac{\partial u}{\partial t} + u\frac{\partial u}{\partial x} = -\frac{1}{\rho}\frac{\partial P}{\partial x} - \frac{f_v\, u}{\rho} \tag{2.1}$$

† University of Montpellier II, CC51, 34095 Montpellier Cedex 5, France

where u and P are the averages (over the cross section of the artery) of the velocity along the x-direction and the pressure (relative to that outside the duct) pressure respectively, A is the area of the cross section, ρ is the blood density and $f_v\ u/\rho$ stands for the viscous drag. Assuming that the velocity and pressure fluctuations are small enough to neglect non-linear terms and introducing the state equation of the artery $A = A(P)$, we obtain

$$\frac{\partial P}{\partial t} + \frac{A}{A'}\frac{\partial u}{\partial x} = 0, \qquad \frac{\partial u}{\partial t} + \frac{1}{\rho}\frac{\partial P}{\partial x} + \frac{f_v\ u}{\rho} = 0 \tag{2.2}$$

where A' stands for the derivative of the cross-sectional area with respect to the pressure ($A' \equiv dA/dP$), that is, the compliance. The non-linear formulation (2.1), although more general than (2.2), suffers from several drawbacks. Indeed, since it has to be solved in the time domain, the viscous-drag term must be assessed by using the Poiseuille assumption for the velocity profile instead of the more accurate frequency-dependent Womersley (1955) solution. Moreover, any viscoelastic wall behavior is difficult to account for since A' may depend on the frequency of the perturbation in this case. In contrast, the linear formulation (2.2) can be solved in Fourier space, and the abovementioned physical behavior (frequency-dependent velocity profile and viscoelasticity) can be included without difficulty. Consistently, Reuderink *et al.* (1989) have shown that better overall accuracy is obtained by using the linear formulation. In the course of the present study, u and P will be taken as the solution of (2.2).

Considering a sector whose diameter and compliance do not depend on the space variable x and letting $P = \hat{P}\exp(-j\omega t)$ and $u = \hat{u}\ \exp(-j\omega t)$, where $j^2 = -1$ and ω is the angular frequency of the wave, the classical wave equation $d^2\hat{P}/dx^2 + k^2\hat{P} = 0$ can be easily derived, the complex wave number being $k = \sqrt{\omega(\rho\omega + jf_v)A'/A}$ and the wave speed being $c = \omega/k$. The general solution within a homogeneous segment is then

$$\hat{P} = P^+\ e^{jk(x-x_0)} + P^-\ e^{-jk(x-x_0)}, \qquad \hat{u} = \frac{k}{\rho\omega + jf_v}\left(P^+\ e^{jk(x-x_0)} - P^-\ e^{-jk(x-x_0)}\right) \tag{2.3}$$

where x_0 is the abscissa of the left boundary of the sector and P^+ and P^- correspond to the amplitude of the forward and backward pressure waves. Their values are determined to satisfy the boundary conditions at $x = x_0$ and $x = x_0 + L$, where L is the length of the sector.

2.2. *Modeling the endovascular stenting*

To model the wave reflexion induced by an endovascular stent placed in an elastic artery, three successive homogeneous segments are considered, each having its own set of constant area and compliance (see figure 1). Each physical quantity in sector number i ($i = 1, 2, 3$) is denoted by index i. Conservation of the total flow rate and energy at the interfaces $1-2$ and $2-3$ requires, for $j = 1, 2$:

$$A_j\hat{u}_j(x_{0_j} + L_j) = A_{j+1}\hat{u}_{j+1}(x_{0_{j+1}}), \qquad \hat{P}_j(x_{0_j} + L_j) = \hat{P}_{j+1}(x_{0_{j+1}}). \tag{2.4}$$

Two boundary conditions, at $x = x_{0_1} = 0$ and $x = x_{0_3} + L_3$, are needed to close the problem. To assess the stent response without spurious wave reflexion, non-reflecting boundary conditions are prescribed at both sides, leading to $P_1^+ = 1$ and $P_3^- = 0$. The four remaining wave amplitudes, viz. $P_2^+, P_3^+, P_1^-, P_2^-$, are determined by solving (2.4) for $j = 1, 2$. The complex coefficient of wave reflexion due to the stent is then defined as

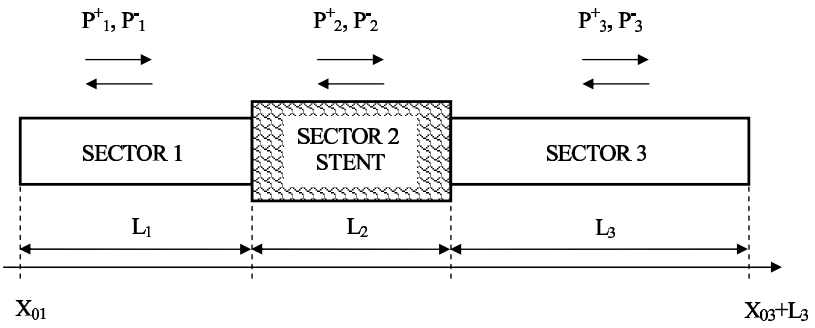

FIGURE 1. Schematic of the three homogeneous sectors used to model an artery stenting in terms of waves.

$R_{\text{stent}} = \exp(-2jk_1L_1)P_1^-/P_1^+$. After some algebra we find

$$R_{\text{stent}} = \frac{A_2K_2(A_1K_1 - A_3K_3)\cos(k_2L_2) - j(A_1K_1A_3K_3 - (A_2K_2)^2)\sin(k_2L_2)}{A_2K_2(A_1K_1 + A_3K_3)\cos(k_2L_2) - j(A_1K_1A_3K_3 + (A_2K_2)^2)\sin(k_2L_2)} \quad (2.5)$$

where $K_i = k_i/(\rho\omega + jf_{v_i})$. A typical value of the speed of propagation of waves in (human) arteries being a few meters per second, the wavelength is usually a few meters. On the other hand, the length scale of the stent is most likely equal to a few centimeters, meaning that the numerical value of the dimensionless parameter k_2L_2 is small compared to unity. Moreover, since the goal of this study is to assess the wave reflexion related to the endovascular prosthesis, one can assume that there is no reflexion in the absence of a stent, i.e. when $A_1K_1 = A_3K_3$ (in other words, we assume that the host artery is perfectly homogeneous). Finally, we obtain the following first-order expression for the reflexion coefficient:

$$R_{\text{stent}} = \frac{j(1-\Lambda^2)}{2\Lambda}k_2L_2 + O((k_2L_2)^2), \qquad \Lambda = \frac{A_1K_1}{A_2K_2} \quad (2.6)$$

This relation shows that the theoretical reflexion induced by an endovascular prosthesis decreases with the length of the stent and increases with the frequency of the wave. Moreover the reflexion coefficient is zero when $\Lambda = 1$, i.e. $A_1K_1 = A_2K_2$. Assuming that viscous effects can be neglected in the reflexion process makes Λ and k_2 real numbers with $\Lambda = \sqrt{A_1A_1'/A_2A_2'}$ and $k_2L_2 = \omega\sqrt{\rho A_2'/A_2}L_2$. Equation (2.6) then leads to a convenient formula to assess the amount of wave reflexion:

$$R_{\text{stent}} \simeq j\omega\sqrt{\rho}\,\frac{A_2A_2' - A_1A_1'}{2\sqrt{A_1A_1'}}\,\frac{L_2}{A_2}. \quad (2.7)$$

From this relation, the amount of wave reflexion is related to the geometrical/mechanical mismatch induced by the stenting and to a stent shape factor L_2/A_2, as well as to the flow conditions. Moreover, it shows that a stent satisfying the relation $A_2 = A_1A_1'/A_2'$ produces no wave reflexion. The compliance A_2' of the stent being always smaller than the compliance A_1' of the host artery, it follows that overdilation ($A_2 > A_1$) tends to reduce the amount of reflected waves. For physiological and mechanical data obtained from animal experimentation (see section 3.3), we find out that the modulus of R_{stent} is not larger than a few percent.

3. Numerical approach

The simple 1D analysis provided in section 2 cannot be used to gain insights about the details of the fluid motion modifications related to the artery stenting. Of significant interest are the perturbations in wall shear stress induced by the compliance mismatch. In the 1D description of the blood flow, the shear stress is modeled by assuming that the shape of the velocity profile is known. Such knowledge is attainable only when the flow is varying weakly along the streamwise direction. However, in the case of stenting, no reasonable assumption regarding the shape of the velocity profile within the transition area can be formulated *a priori* and the multi-dimensional flow equations must be solved.

The incompressible unsteady Navier-Stokes equations are solved by the NSIKE code developed at University of Montpellier and INRIA by Medic & Mohammadi (1999). The solver is based on the projection method of Chorin (1967) with finite element discretization. A third order low storage Runge-Kutta approach is used for the time-stepping. At each sub steps, the computation of the intermediate velocity is done explicitly and the stabilization of the convection terms is based on the Positive Streamwise Invariant (PSI) residual distribution scheme proposed proposed by Deconinck *et al.* (1993) and Paillere, Carette & Deconinck (1994). Specifically, a mixed Galerkin/PSI formulation has been used in order to minimize the numerical dissipation while ensuring the stability of the solution. Moving boundaries are accounted for by the Arbitrary Lagrangian Eulerian formulation. This code has been extensively validated by Medic & Mohammadi (1999), who computed classical test cases such as the flow over a 2D flat plate, within a closed cavity, and over a backward-facing step. Specific unsteady test cases have been performed in the course of this study, two of which are presented in sections 3.1 and 3.2. The numerical setup used to study the effects of the endovascular stenting is then described in section 3.3.

3.1. *Pulsed pipe flow*

We consider the pulsatile flow of an incompressible Newtonian fluid (kinematic viscosity ν) within a rigid, straight circular pipe of radius R_0 and length L. For a pulsed flow rate of the form $Q(t) = Q_0 + Q_1 \exp(j\omega t)$, where ω is the pulsation and Q_0 and Q_1 stand for the steady and pulsed parts of the flow rate, the (complex) velocity profile may be written following Womersley (1955) as

$$u(r,t) = \frac{2Q_0}{A_0}\left(1 - \frac{r^2}{R_0^2}\right) + \frac{Q_1}{A_0}\frac{1 - \frac{J_0(\alpha r/R_0)}{J_0(\alpha)}}{1 - \frac{2J_1(\alpha r/R_0)}{\alpha J_0(\alpha)}} \tag{3.1}$$

where $A_0 = \pi R_0^2$ is the cross section area and $\alpha = j^{3/2}W_0$, where $W_0 = R_0\sqrt{\omega/\nu}$ is the Womersley parameter. Due to the incompressibility constraint, the solution does not depend on the abscissa x along the pipe. The present test case consists in imposing the velocity profile (3.1) at the inlet of the computational domain ($x = 0$) together with a zero-pressure boundary condition at the outlet ($x = L$), and checking the ability of the code to preserve the analytical solution throughout the pipe. Starting with a zero-velocity, constant-pressure field, four cycles were computed in order to reach a proper periodic state. The results shown correspond to $L/R_0 \simeq 53$ and $W_0 \simeq 10.63$. The mean bulk Reynolds number based on R_0 and Q_0/A_0 is $R_b = 320$ while the flow-rate ratio is $Q_1/Q_0 = 0.5$. Under these conditions, the flow reverses. The numerical solution obtained by solving the Navier-Stokes equations in cylindrical form with a mesh of 169×21 grid points (169 nodes in x, 21 along the radial direction r) is virtually 1D (no dependence

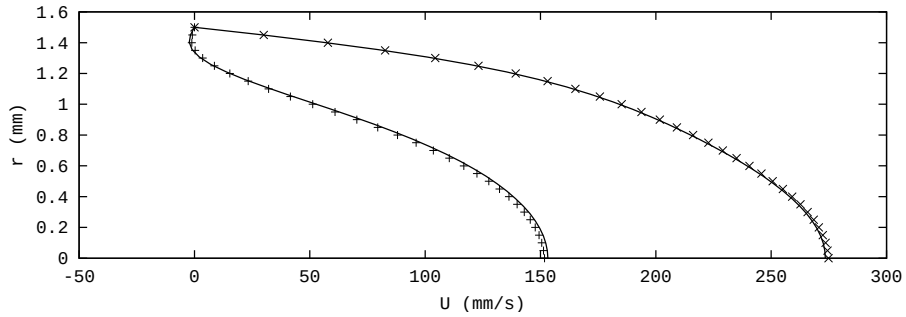

FIGURE 2. Analytical (lines) and numerical (symbols) velocity profiles at ×:systole and +:diastole.

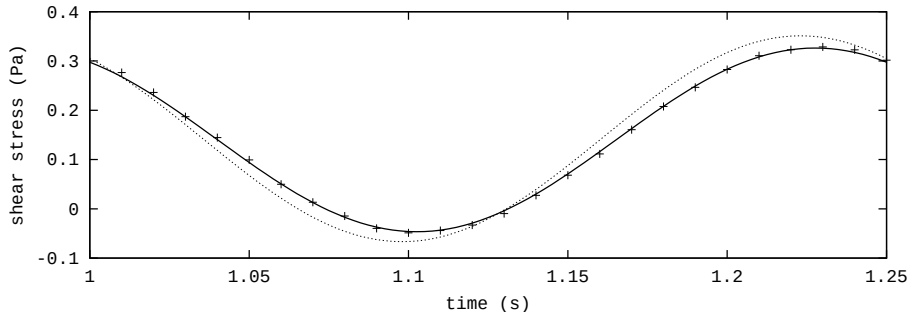

FIGURE 3. Analytical (lines) and numerical (symbols) wall shear stress as a function of time. ——— , finite differences applied to (3.1); ····· , analytical differentiation of (3.1).

along the longitudinal coordinate x, not shown). The overall comparison between analytical and numerical velocity profiles is good, as shown in figure 2. Eventually, the wall shear stress obtained numerically is in good agreement with that expected over the period of time. Figure 3 shows that the agreement between the wall shear stress given by the numerical solution and that obtained by formally differentiating (3.1) is fairly good (less than 10 % error). The agreement becomes virtually perfect when the gradient of the analytical profile (3.1) is evaluated using second-order finite differences with the same resolution as that used in the simulation.

3.2. *Wall-induced channel flow*

The computational domain now extends from $x = 0$ to $x = 25$ streamwise and from $y = 0$ to $y = h$ cross stream. A symmetry condition is imposed at both boundaries $x = 0$ and $y = 0$ while zero pressure is prescribed at the section $x = 25$. The boundary at $y = h$ is a moving straight

wall which remains parallel to the x-axis and whose (complex) position as a function of time t is given by $h(t) = h_0(1 + \epsilon e^{-j\omega t})$. In this expression, h_0 is the mean distance between the wall and the symmetry plane $y = 0$ and ϵ fixes the amplitude of the wall oscillation. Seeking a stream function of the form $\Psi = xF(\eta)e^{-j\omega t}$, where η is the reduced coordinate $\eta = y/h(t)$, one may derive the following equation for the function F:

$$F'''' + \frac{h'h}{\nu}(\eta F''' + 2F'') + \frac{j\omega}{\nu}h^2F'' = 0. \tag{3.2}$$

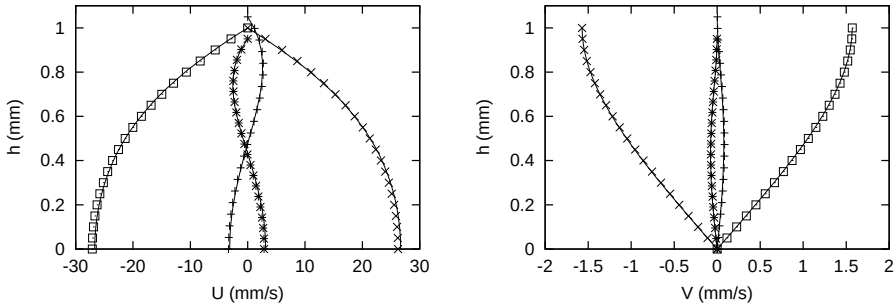

FIGURE 4. Analytical (symbols) and numerical (lines) streamwise (left) and normal wise (right) velocity profiles at times +, $t = 0$; $\times$, $t = T/4$; $*$, $t = T/2$ and $\square$, $t = 3T/4$.

Recall that the velocity components are given by $u = \partial\Psi/\partial y$ and $v = -\partial\Psi/\partial x$ so that the boundary conditions $v(x,0) = \partial u/\partial y(x,0) = 0$, $u(x,h) = 0$ and $v(x,h) = h' = -j\omega\epsilon h_0 e^{-j\omega t}$ lead to $F(0) = F''(0) = 0$, $F'(1) = 0$ and $F(1) = j\omega\epsilon h_0$ respectively. Expanding F as power series of the (small) parameter ϵ, viz. $F/\epsilon = F_0 + \epsilon F_1 + O(\epsilon^2)$ leads to the following first order solution

$$F_0 = j\omega h_0 \frac{\eta - \sinh(\alpha\eta)/\alpha\cosh\alpha}{1 - \tanh(\alpha)/\alpha} \tag{3.3}$$

where $\alpha = j^{3/2}W_0$ is proportional to the Womersley parameter $W_0 = h_0\sqrt{\omega/\nu}$. Figure 4 shows the comparison between the first-order analytical solution and the numerical profiles for $x = 11.875$, $\epsilon = 0.05$ and $W_0 = 2.8$. The agreement is good for the four phases considered which correspond to the uppermost position ($t = 0$), the most negative wall speed ($t = T/4$), the wall bottom position ($t = T/2$) and the maximum wall speed ($t = 3T/4$) respectively. Note that for the values of the parameters selected, the first-order correction ϵF_1 is negligible compared to F_0 so that the approximate solution, (3.3) is relevant to the test case.

3.3. *Computational domain*

Since our objective is to investigate the global effect of the compliance mismatch induced by stenting, the endovascular prosthesis is modeled as a uniform duct (the details of the struts are not represented) whose wall is not compliant. Such a "prosthesis" is inserted within an elastic artery with compliant wall, as shown in figure 5. We suppose that the computational domain is sufficiently short to neglect any variation of the host artery characteristics. Moreover, the flow rate entering the domain is taken similarly to section 3.1, viz. $Q(x_{\rm inlet}, t) = Q_0 + Q_1\exp(j\omega(t - x_{\rm inlet}/c))$, where ω is the pulsation, $x_{\rm inlet}$ is the abscissa of the inlet section, and Q_0 and Q_1 stand for the steady and pulsed parts of the flow rate. The mechanical and geometrical data were obtained from animal experimentation performed by Vernhet *et al.* (2001): the angular frequency is $\omega = 8\pi$ (only the first harmonic of the temporal evolution of the flow rate is kept as a first approximation), the mean artery radius is $R_0 = 1.5$ mm, the distensibility coefficient of the non-stented artery is $A'/A = 20.7 \times 10^{-6}\ Pa^{-1}$ and the length of the stent is set to $L_{\rm stent} = 13$ mm. At the stent level, the compliance measured is small enough (six times smaller than in the host vessel) to be neglected in this exploratory study (rigid prosthesis).

In the real world, the motion of the vessel boundary results from the coupling between

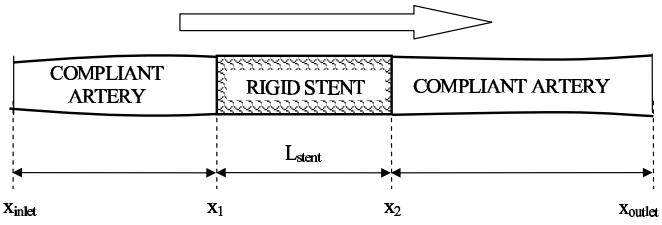

FIGURE 5. Schematic of the computational domain.

the fluid and wall mechanics and the local radius is related mainly to the pressure field. Such a coupling is difficult to handle, because the density of blood and tissue are of the same order and the rheology of the vessels is far from well understood. Besides, we are mostly interested in the response of the fluid mechanics to wall-motion perturbations induced by the compliance mismatch. In this framework, the fluid/wall coupling problem can be avoided by prescribing the wall motion *a priori*. Since the flow rate is harmonic with angular frequency ω, the wall displacement for an elastic uniform artery without reflexion may be written as

$$R(x,t) = R_0 \left(1 + \epsilon e^{j(\omega t - kx)}\right) , \qquad k = \frac{\omega}{c}, \tag{3.4}$$

where the wave number k is related to the speed of the (forward) pressure wave c. The animal experimentation of Vernhet *et al.* (2001) suggests $\epsilon = 0.05$, meaning that the amplitude of the wall displacement is close to $2\epsilon R_0 = 0.15$ mm. The speed of propagation is chosen real (no viscous-damping effect accounted for). Moreover, its real part is fixed by stating that, the non-stented artery being uniform along the streamwise direction, the mass-flow rate at any section $x = L$ should be the time-lagged version of the mass flow rate at $x = x_{\text{inlet}}$. The conservation of mass applied to the artery sector $0 < x < L$ then implies that:

$$Q_1 e^{j\omega(t-(x_{\text{inlet}}+L)/c)} = Q_1 e^{j\omega(t-x_{\text{inlet}}/c)} + 2\pi \int_{x_{\text{inlet}}}^{x_{\text{inlet}}+L} R\frac{dR}{dt}dx \tag{3.5}$$

Making use of (3.4) and keeping only first-order terms in ϵ to assess the integral in (3.5), we obtain the following expression for the speed of propagation of the pressure wave:

$$c = \frac{Q_1}{2A_0\epsilon} + O(1) , \qquad A_0 = \pi R_0^2 \tag{3.6}$$

From the physiological data obtained by Vernhet *et al.* (2001), the following values were used for the flow rate: $Q_0 \simeq 2413$ mm^3/s and $Q_1 \simeq 1761$ mm^3/s. Equation (3.6) then leads to $c \simeq 2492$ mm/s. With $\omega = 8\pi$, the corresponding wavelength is $\lambda \simeq 623$ mm. In the case where the vessel is stented between abscissae x_1 and x_2 (see figure 5), the wall displacement is zeroe (fully rigid stent) for $x_1 < x < x_2$:

$$R(x,t) = R_0 \left(1 + \epsilon\, f(x)\, e^{j(\omega t - kx)}\right) \tag{3.7}$$

where the damping function is $f(x) = [1 - \tanh(x - x_1)]/2$ for $x < (x_1 + x_2)/2$ and $f(x) = [1 + \tanh(x - x_2)]\exp(jk(x_2 - x_1))/2$ for $x > (x_1 + x_2)/2$. Equation (3.7) gives the wall displacement for an elastic stented artery, assuming that the speed of propagation within the prosthesis is infinite (since the wall is not compliant). Note that L_{stent}/λ

being very small, (2.7) can be used to estimate the reflexion coefficient under the mechanical conditions considered. This latter relation leads to $|R_{\rm stent}| \simeq 2$ %. As a result, the pressure field is related mostly to the forward pressure wave, which justifies the fact that no backward-propagating wave is accounted for in (3.7). Besides, the length of the transition zone between the elastic artery and the stent is of order 3 mm (this is a direct consequence of the damping function $f(x)$ used in 3.7). This value is in agreement with the observations made during the animal experimentations of Vernhet *et al.* (2001) and showing that the buffer region is close to one diameter long. Finally, the radius of the non-compliant prosthesis is set to the medium artery radius R_0 (no overdilation). An over dilated prosthesis can be represented by the following wall displacement:

$$R(x,t) = R_0 \left(1 + \epsilon\, f(x)\, e^{j(\omega t - kx)}\right) + (1 - f(x))\delta R_{\rm stent} \tag{3.8}$$

where the damping function is defined as in (3.7) and $\delta R_{\rm stent}$ is the amount of overdilation.

4. Numerical results

Several 2D axisymmetric simulations have been performed, based on the computational domain and wall motion described in section 3.3. In all cases, the bulk Reynolds number based on the steady part of the flow rate Q_0 and the mean radius R_0 is close to $R_b = 102$. The Womersley number is $W_0 = 3.36$. The velocity profile is imposed at the inlet section $x = x_{\rm inlet}$ following the (complex) Womersley solution in elastic tubes:

$$u_{\rm inlet} = \frac{2Q_0}{\pi R(x_{\rm inlet},t)^2}\left(1 - \frac{r^2}{R(x_{\rm inlet},t)^2}\right) + \frac{Q_1}{\pi R(x_{\rm inlet},t)^2}\frac{1 - J_0(\alpha y)/J_0(\alpha)}{1 - 2J_1(\alpha)/\alpha J_0(\alpha)} e^{j\omega(t - x_{\rm inlet}/c)}$$

$$v_{\rm inlet} = j\omega\epsilon R_0 \frac{y - 2J_1(\alpha y)/\alpha J_0(\alpha)}{1 - 2J_1(\alpha)/\alpha J_0(\alpha)} e^{j\omega(t - x_{\rm inlet}/c)} \tag{4.1}$$

where $y = r/R(x,t)$ is the reduced radial coordinate ($0 \le y \le 1$). A zero-constraint condition is used at the outlet section $x = x_{\rm outlet}$. In order to assess the effect of the inlet/outlet boundary conditions on the results, computational domains with two different lengths have been considered. Two different spatial resolutions were also used, to assess the spatial discretization errors. The main characteristics of the calculations performed are given in table 1 where Δx is the grid spacing in the streamwise direction in the area $x_1 < x < x_2$ and Δr refers to the grid spacing in the radial direction. Runs R1 and R2 correspond to reference calculations without endovascular prosthesis, the artery being fully rigid (no wall displacement) for R1 and elastic for R2. Labels R3 and R4 correspond to runs with stenting, the overdilation being non-zero only for the latter where $\delta R_{\rm stent} = \epsilon R_0$ (the stent radius is equal to the artery radius at systole). When present, the stent is between $x_1 = 34$ mm and $x_2 = 47$ mm. Runs whose label contains 'a' have been performed with a longer computational domain than others. Labels containing letter 'b' correspond to runs with finer mesh in the radial direction. In all cases, four cardiac cycles were computed first, in order to reach a periodic state. A fifth cycle was then computed in order to analyze the results and compare the different physical/numerical configurations.

Time evolutions of the flow rate at inlet and outlet sections are shown in figure 6 for case R2. The constraint that was introduced in section 3.3 in order to set the speed of propagation of the pressure wave is fulfilled satisfactorily. Indeed, the flow rate at $x = x_{\rm outlet}$

Run	Wall motion	η	δR_{stent}	x_{inlet}	x_{outlet}	Δx	Δr	# of grid points
R1	$R(x,t) = R_0$	0.0	N/A	0	80	0.075	0.286	3528
R2	(3.4)	0.05	N/A	0	80	0.075	0.286	3528
R3	(3.7)	0.05	0.0	0	80	0.075	0.286	3528
R4	(3.8)	0.05	0.075	0	80	0.075	0.286	3528
R2a	(3.4)	0.05	N/A	−30	110	0.075	0.286	4368
R3a	(3.7)	0.05	0.0	−30	110	0.075	0.286	4368
R3b	(3.7)	0.05	0.0	0	80	0.050	0.286	5208

TABLE 1. List of the axisymmetric calculations performed, with their main numerical characteristics and the equations governing the wall motion. Lengths and abscissae are in mm.

is the signal at $x = x_{\text{inlet}}$ with a time lag close to $(x_{\text{outlet}} - x_{\text{inlet}})/c \simeq 80/2492 \simeq 0.032$s. In absence of an endovascular prosthesis, all the physical quantities are self-similar, with a constant speed of propagation c along the computational domain. Due to the wall displacement (3.4), the wall shear stress is not constant in the streamwise direction, as shown in figure 7 at four different instants. Instead it alternately increases and decreases along the domain, depending on the phase considered. Note that the harmonic displacement (3.4) is never apparent, because the length of the computational domain (80 mm) is small compared to the wavelength (see also figure 9, top row). In spite of this, the numerical solution depends only weakly on the length of the whole domain, as shown in figure 8, which compares the wall shear stress from runs R2 and R2a. Only small disagreement is visible, close to the upsstream end of the R2 domain (the smallest one). There is virtually no difference between the two runs in the central region. The same conclusion can be drawn in the case of a stented artery by comparing runs R3 and R3a (not shown). Thus, regarding the effects of the vessel stenting, the numerical results do not depend on the details of the implementation of the boundary conditions. In the case where the vessel is not compliant, there should be no time lag between shear-stress signals at different locations, because the exact Womersley profile is imposed at $x = x_{\text{inlet}}$. Accordingly, the wall shear stress is mainly uniform over the streamwise distance in case R1 (see figure 7).

The shape of the computational domain for cases R2, R3 and R4 is shown in figure 9 for times $t = nT$ (corresponding to systole at the inlet section) and $t = (n+1/2)T$ (diastole). The non-compliant region which represents the endovascular prosthesis is clearly visible (cases R3 and R4) in the central region. However, the over-dilated stent (R4) is hardly visible at systole since $\delta R_{\text{stent}} = \epsilon R_0$ in this case. The contours of streamwise velocity show that the flow accelerates when the cross-sectional area decreases. The effect of the wall-motion mismatch on the wall shear stress is shown in figure 10. At systole, this quantity is larger in the medium part of the stented region ($x \simeq 40$ mm) than in the

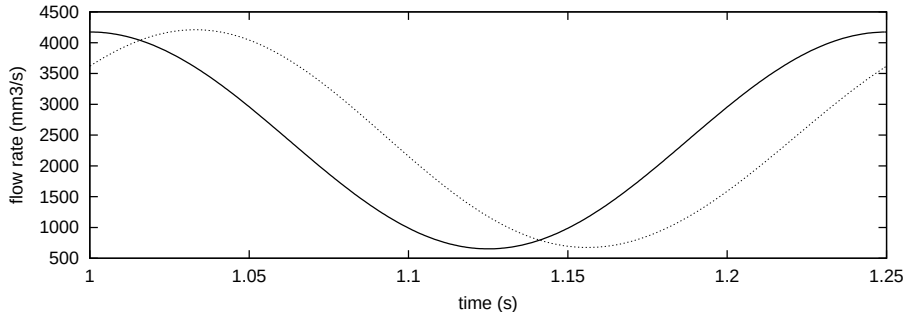

FIGURE 6. Time evolutions of the flow rate at sections ——— : $x = x_{\text{inlet}}$ and ····· : $x = x_{\text{outlet}}$ for the case R2.

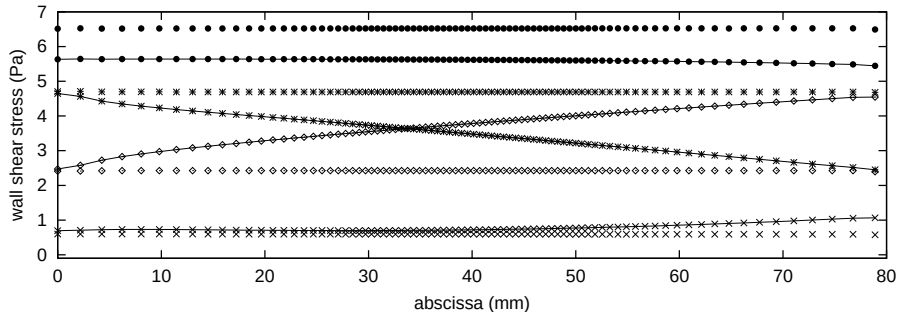

FIGURE 7. Wall shear stress for runs R1 (symbols) and R2 (lines with symbols) at times: $\bullet : t = nT$, $\diamond : t = (n + 1/4)T$, $\times : t = (n + 1/2)T$ and $* : t = (n + 3/4)T$.

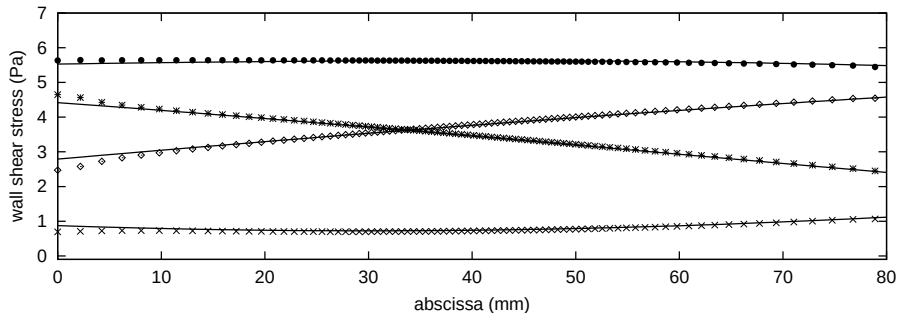

FIGURE 8. Wall shear stress for runs R2 (symbols) and R2a (———) at times: $\bullet : t = nT$, $\diamond : t = (n + 1/4)T$, $\times : t = (n + 1/2)T$ and $* : t = (n + 3/4)T$.

non-stented artery. This is consistent with the fact that the cross-sectional area in R3 and at systole is smaller in the prosthesis zone (see figure 9). At diastole, the cross-sectional area within the stent is larger and the wall shear stress is smaller. In the transition zones between the endovascular prosthesis and the elastic artery, the stress experiences larger fluctuations, especially at systole. Extra stress is generated in the upstream transition zone, which acts as a convergence ($x \simeq 35$ mm). Conversely, the downstream buffer region acts as a divergence at systole and tends to decrease the stress. Accordingly, the wall shear stress turns out to be locally smaller than its value in the non-stented artery ($x \simeq 47$ mm). The transition zones have less effect at diastole, when the flow rate is

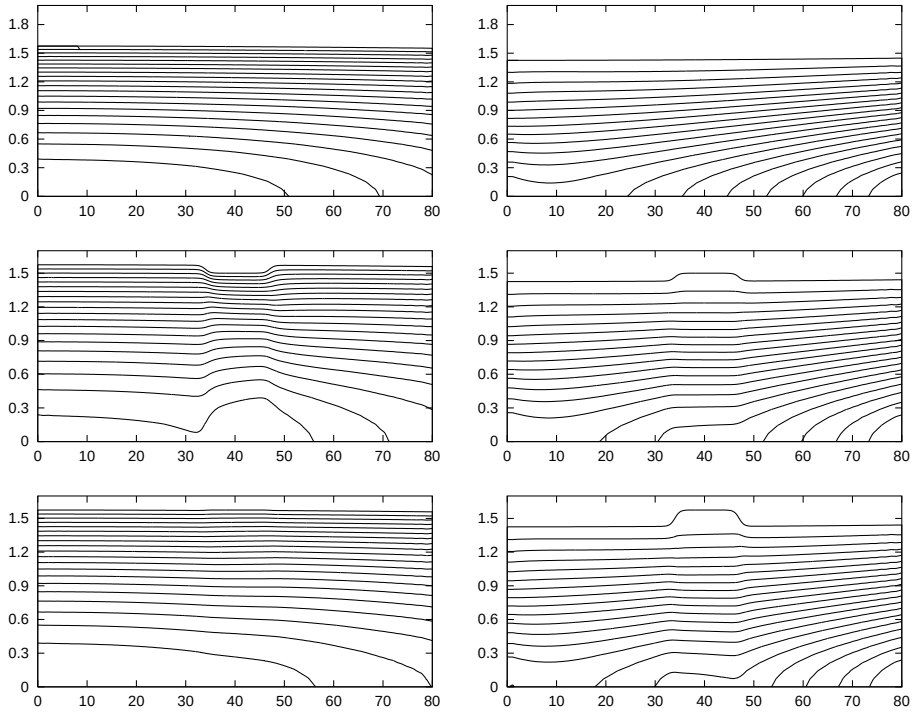

FIGURE 9. Shape of the computational domain at systole (left column) and diastole (right column) for the runs R2 (top row), R3 (medium row) and R4 (bottom row). The isolines of the streamwise velocity are plotted. The streamwise and radial coordinates are expressed in millimeters. The aspect ratio R_0/L has been multiplied by 35 for convenience.

smaller. Note finally that using a finer mesh produces only small changes in wall shear stress (compare runs R3 and R3b). Thus the numerical errors are much smaller than the physical effects related to the stent. Figure 11 shows the time dependence of the stress near $x = (x_1 + x_2)/2 \simeq 40$ mm. The amplitude of this quantity over the cardiac cycle is larger for the stented vessel than for the elastic artery. It is worth noting that although the length of the stent is very small compared to the wavelength, the amplitude of the wall shear stress in case R3 behaves more like case R1 (fully rigid tube) and less like case R2 (elastic tube). The over-dilated prosthesis, by avoiding the increase in shear stress at systole (there is no geometry discontinuity at systole for the case R4; see figure 9), drastically limits the increase in stress amplitude.

5. Conclusions

This theoretical/numerical study suggests that over-dilated stents produce less hemodynamic perturbations. From the pressure-wave point of view, the optimal overdilation is proportional to the compliance ratio. Moreover, because the reflexion coefficient is proportional to the stent-to-wavelength ratio, it is most likely that the amount of wave reflexion remains rather small. An easy-to-use formula is provided to estimate the reflexion coefficient from knowledge of the compliance before and after stenting. From the local hemodynamic point of view, the amplitude of the wall shear stress is drastically increased (by 45-50 % at the stent level, possibly more in the transition regions) by

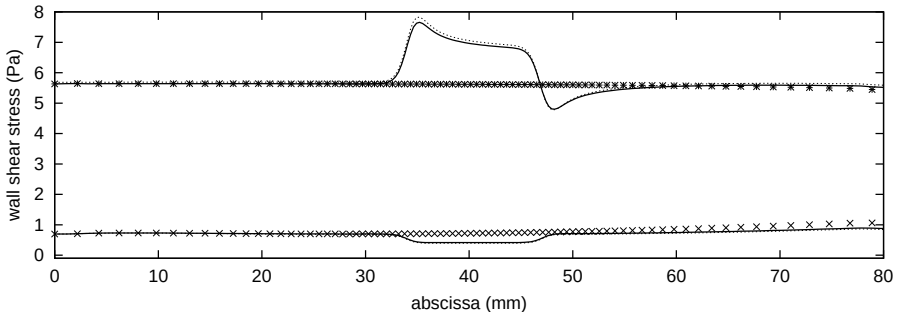

FIGURE 10. Wall shear stress for runs R2 (symbols), R3 (———) and R3b (·····) at times $*$:$t = nT$ and $\times$:$t = (n + 1/2)T$

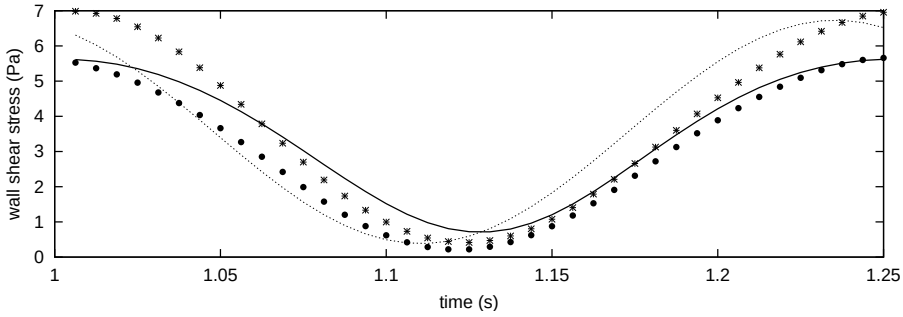

FIGURE 11. Wall shear stress versus time for runs ····· : R1, ——— : R2, $*$:R3 and $\bullet$:R4 at $x \simeq 40$ mm.

stenting. This result supports the idea that stenting can induce endothelial dysfunction via hemodynamic perturbations. The amplitude of the fluctuations in wall shear stress over the cardiac cycle are not as large when a (slight) over-dilatation is used.

REFERENCES

CHORIN, J. A. 1967 A numerical method for solving incompressible viscous flow problems. *J. Comp. Phys.* **2**, 12–26.

DAVIES, P., SHI, C., DEPAOLA, N., HELMKE, B. & POLACEK, D. 2001 Hemodynamics and the focal origin of atherosclerosis. A spatial approach to endothelial structure, gene expression, and function. *Annu. N.Y. Acad. Sci.* **947**, 7–16.

DECONINCK, H., STRUIJS, R., BOURGOIS, G. & ROE, P. 1993 *Compact advection schemes on unstructured grids.* Von Karman Inst. Lecture Series 1993-04.

HUGHES, T. & LUBLINER, J. 1973 On the one-dimensional theory of blood flow in the larger vessels. *Math. Biosci.* **18**, 161–170.

MEDIC, G. & MOHAMMADI, B. 1999 NSIKE – an incompressible Navier-Stokes solver for unstructured meshes. *INRIA Res. Rept.* 3644.

PAILLERE, J-C., CARETTE, C. & DECONINCK, H. 1994 *Multidimensional upwind and SUPG methods for the solution of the compressible flow equations on unstructured grids.* VKI Lecture Series 1994-05.

RAU, T., SCHOFER, J., SCHLUTER, M., SEIDENSTICKER, A., BERGER, J. & MATHEY,

D.G. 1998 Stenting of non acute total coronary occlusions: predictors of late angiographic outcome. *J. Am. Coll. Card.* **31**, 275–280.

Reuderink, P. J., Hoogstraten, H. W., Sipkema, P., Hillen, B. & Westerhof, N. 1989 Linear and nonlinear one-dimensional models of pulse wave transmission at high Womersley numbers. *J. Biomech.* **22**, 819–827.

Rolland, P. H., Charifi, A. B. & Verrier, C. 1999 Hemodynamics and wall mechanics after stent placement in swine illiac arteries: comparative results from six stent designs. *Radiology* **213**, 229–246.

Vernhet, H., Demaria, R., Oliva-Lauraire, M. C., Juan, J. M., Sénac, J. P. & Dauzat, M. 2001 Changes in wall mechanics after endovascular stenting in rabbit aorta: comparison of three different stent designs. *Am. J. Roent.* **176**, 803–807.

Vernhet, H., Juan, J.M., Demaria, R., Oliva-Lauraire, M.C., Sénac, J.P. & Dauzat, M. 2000 Acute changes in aortic wall mechanical properties after stent placement in rabbits. *J. Vasc. Inter. Rad.* **11**, 634–638.

Womersley, J.R. 1955 Oscillatory motion of a viscous liquid in a thin-walled elastic tube–I: The linear approximation for long waves. *Phil. Mag. (Series 7)* **45**, 199–221.